Mechanical and thermal performance of additively manufactured copper, silver, and copper-silver alloys

John Robinson[1,2*], Arun Arjunan[1], Ahmad Baroutaji[1] and Mark Stanford[1]

[1]Additive manufacturing of Functional Materials (AMFM) research group, School of Engineering, University of Wolverhampton, Telford Innovation Campus, Telford TF2 9NT, UK

[2]Additive Analytics Ltd., Stirchley Road, Telford TF3 1EB, UK

Abstract

On-demand additive manufacturing (3D printing) offers great potential for the development of functional materials for the next generation of energy-efficient devices. In particular, novel materials suitable for efficient dissipation of localised heat fluxes and non-uniform thermal loads with superior mechanical performance are critical for the accelerated development of future automotive, aerospace, and renewable energy technologies. In this regard this study reports the Laser Powder Bed Fusion (L-PBF) processing of high purity (>99%) copper (Cu), silver (Ag) and novel copper-silver (CuAg) alloys ready for on-demand additive manufacturing (AM). The processed materials were experimentally analysed for their relative density, mechanical and thermal performance using X-ray computed tomography (X-CT), destructive tensile testing and Laser Flash Apparatus (LFA) respectively. It was found that while Ag featured higher failure strains, Cu in comparison showed a 109%, 17% and 59% improvement in yield strength (σ_y), Youngs Modulus (E) and ultimate tensile strength (UTS) respectively. As such the σ_y, E and UTS for L-PBF Cu is comparable to commercially available L-PBF Cu materials. CuAg alloys however significantly outperformed Ag, Cu, and all commercial Cu materials when it came to mechanical performance offering significantly superior performance. The σ_y, E and UTS for the novel CuAg composition were 105%, 33% and 94% higher in comparison to Cu. Although slightly different, the trend continued with a 106% and 91% rise for σ_y and UTS respectively for CuAg in comparison to industry-standard Cu. Unfortunately, E values for industry-standard Cu alloys were not available. When it came to thermal performance, L-PBF Ag was found to offer a 70% higher thermal diffusivity in comparison to Cu despite the variation in density and porosity. CuAg alloys however only showed a 0.8% variation in thermal performance despite a 10% to 30% increase in Ag. Overall, the study presents a new understanding regarding the 3D printing and performance of Cu, Ag and CuAg alloys.

Keywords: Thermal performance; Mechanical performance; Diffusivity; L-PBF; Additive Manufacturing; Silver; Copper; Ag; Cu.

[*] Corresponding author: SC120, School of Engineering, University of Wolverhampton
Telford Innovation Campus, Telford, TF2 9NT, UK
Tel.: +44 1902 323958. E-mail address: j.robinson12@wlv.ac.uk (John Robinson)

1. Introduction

Thermal management without sacrificing structural integrity is challenging for many industries and applications where developments in new materials and efficient architecture are still called for [1–3]. This is partly fuelled by interest from industries that are focused on the next generation of consumer electronics, automotive, aerospace, defence, healthcare, and renewable energy sectors [4–6]. When it comes to heat transfer even small improvements can have a significant impact on cooling [7] and efficient thermal management drastically reduces material waste while increasing component reliability and life [8]. Additionally emerging systems such as those in electric vehicles (EVs), radio-frequency systems, high power light-emitting diodes, solar cells and solid-state laser light sources all have significant heat dissipation requirements [8–10] and therefore it is widely agreed that the localised high heat fluxes and non-uniform heat dissipation requirements for many industries will require advances in materials and manufacturing technologies to effectively dissipate the thermal loads for future systems and devices [1,4].

Additive manufacturing (AM) is at the forefront of potential technologies that can enable high-efficiency thermal management devices [11–13] through improved geometry, materials and metamaterials with high heat transfer properties [7,14,15]. AM technologies fabricate parts in a layer-by-layer process rather than machining (subtracted) or forming material as with more traditional manufacturing technologies. Today layer by layer manufacturing techniques encompass many processing technologies (extruding, jetting, polymerisation, sheet lamination, spraying and/or thermally fusing) and related materials (filaments, wires, liquids, powders, pastes, and sheet) [4,16–18]. During the AM process material is added to create three-dimensional (3D) components that are defined by digital data [1]. Although the range of materials that can be processed by AM is increasing [19] a recent survey found increasing demand for high-performance metallic alloys from industries including automotive, aerospace and electronics [20]. In this regard, one of the most promising AM technologies suitable for the creation of complex metallic components is Laser Powder Bed Fusion (L-PBF) [21,22].

The L-PBF process uses a high-powered laser source to selectively laser melt (SLM) powdered metallic materials such as titanium, aluminium, steels and Inconel [23–26] to achieve densities above 99.9% [27,28]. The L-PBF process is complex and the processing is dependent on laser diffusion, scattering, heat transfer, material absorptivity, phase transformation, surface tension and fluid flow associated with the powder and molten material [23]. This gives rise to a significant number of process variables that affect the properties of fabricated components [29]. The L-PBF process is a combination of many (over 130) parametric variables related to feedstock, build environment, process, laser and material interactions [29]. Since material absorptivity and reflectivity are fundamental [23,29] to laser processing, the processing of highly reflective and thermally conductive materials with relatively low power (<400 W) L-PBF technologies is highly challenging [30,31] due to poor energy absorption during the L-PBF process [32]. High purity Cu reflects laser wavelengths of 1000 to 1100 nm [31] and these wavelengths are commonly utilised

in many L-PBF systems. This can result in energy absorption <2% in some cases. Colopi *et al.* [32] reported utilising a 1kW fibre laser for L-PBF of 99.9% Cu. The results concluded that despite the high reflectivity of Cu, the 1060 nm wavelength laser is feasible for copper L-PBF processing. However, due to high reflectivity high laser powers of 600W were required. Accordingly, it has been argued [32] that the 400W fibre lasers commonly found in some L-PBF systems may not have sufficient laser power to process reflective copper and silver. Importantly silver reflects 98.8% laser wavelengths of 650 nm [33], and therefore it is hypothesized that a 400W at 1060 nm wavelength laser may supply the required energy to laser melt Cu, Ag and CuAg alloys.

Ag and Cu exhibit exceptional thermal properties in comparison to other metals. Ag has the highest thermal conductivity and diffusivity performance of any metal at 415 W/mK and 165 mm^2/s followed closely by Cu 397 W/mK and 111 mm^2/s [34] respectively. As such Ag and Cu are seeing increasing research in L-PBF as a base and alloying elements for thermal management [33,35,36]. However, previous studies have reported the requirement of relatively high powered lasers (~1 kW) to achieve acceptable component densities [32]. Furthermore, recent research has reported the highest achievable density of pure Cu with a standard 200W laser is 85.8% [31]. In addition to their pure form, Ag and Cu are also being investigated as alloying elements to exploit their desired properties [37,38] compounding the interest in their potential laser processing. So far L-PBF processing of high purity Ag, Cu and CuAg alloys has seen limited research with varying success [31,39,40].

Highlighting the benefits of Ag, Gohar *et al.* [41] synthesised copper-aluminium-silver (Cu-Al-Ag) alloys through powder metallurgy with varying Ag content and investigated the resultant microstructure, thermal and mechanical properties. The study found that the addition of Ag resulted in increased hardness, compressive strength, and thermal diffusivity. Thermal diffusivity investigations were conducted at room temperature with diffusivity values increasing in an almost linear fashion as Ag content increased from 2% to 6% Ag in 0.5% increments. Thermal diffusivity properties increased from 20.17 mm^2/s for 2% Ag to 26.75 mm^2/s for 6% (wt.) Ag [41]. Sun *et al.* [35] sintered molybdenum-copper-silver (Mo-Cu-Ag) alloys to investigate 0.5% - 2% addition of Ag. The resultant microstructure was found to be homogeneous with electrical and thermal properties increasing with the Ag content. However, it was found that the Ag content had a negligible effect on the coefficient of thermal expansion (CTE) of the material [42]. Although these studies highlight the benefit of Ag as an alloying element for desirable material properties, the manufacturing techniques utilised for alloy fabrication received little investigation. Due to the significant cost differences between pure Ag and Cu; Cu and its alloys are becoming increasingly popular and research is being carried out that utilises the potential benefits of L-PBF technologies [32,36,43]. For example, tungsten-copper (W-Cu) alloys have been investigated utilising L-PBF in several studies [44,45] with the development of Cu-Cr alloys also being reported [46].

It is also worth noting that Cu and its alloys have recently begun to emerge from L-PBF system manufacturers [47] and material development companies [48] with varying compositions and purity [47]. For example, market-leading system manufacturer and material supplier EOS GmbH have recently released three Cu material variants [47]. EOS copper CuCP has Cu purity above 99.95% and is described as an excellent thermal and electrical conductor suitable for electrical motors and inductor applications. EOS CuCrZr is a copper-chromium-zirconium alloy with moderate conductivity properties developed for a rocket engine, inductor coils and heat exchanger applications. Due to increased industry interest, the L-PBF processing of Cu and Cu alloys are receiving much attention, however, the resulting properties and process parameter requirements are yet to be reported. Another trend within the AM industry is the emergence of application-specific L-PBF systems and materials where companies such as Alloyed (UK), Elementum 3D (US) and Metals 4 Print (Germany) are developing bespoke Metal Matrix Composite (MMC) and metallic alloys combining the benefits of L-PBF with materials for specific applications. Additionally, system developers such as Additive Manufacturing Custom Machines (AMCM) offer the potential to create application specific L-PBF systems with larger build areas, higher powered lasers, multiple lasers, and custom process constraints. Consequently, it is envisaged that designers and engineers in the future will have the ability to dictate not only the optimum material for their application but also the most suitable L-PBF methodology for optimum properties. As such the thermal and mechanical performance of highly conductive Ag, Cu and CuAg alloys that can be processed by L-PBF technologies is of great interest to both academia and industries in the emerging field of AM.

For the first time, this study reports the L-PBF fabrication of high purity (>99% purity) Cu, Ag and CuAg alloys and reports the mechanical and thermal properties. The mechanical properties are compared to currently available industry-standard Cu, CuCP and CuCrZr materials to give an insight into the potential industrial applications for these materials. L-PBF Cu and Ag powder composition, morphology and distribution are reported using dynamic imaging, Scanning Electron Microscopy (SEM) and Energy Dispersive X-Ray (EDX) analysis while thermal diffusivity of Cu, Ag and CuAg alloys is reported through Netzsch Laser Flash Apparatus (LFA). Other than limited previous studies [49], CuAg alloy porosity morphology and distribution in comparison with L-PBF Cu and Ag pore defect morphology and distribution are yet to be reported; an aspect described in this study through the use of advanced X-ray Computed Tomography (XCT). Yield strength (σ_y), Youngs Modulus (E), failure strain (ε_f) and ultimate tensile strength (UTS) of Cu and Ag as built structures are also reported in comparison to CuAg alloys.

2. Material and methods

2.1. Additive manufacturing

The samples investigated in this study were fabricated using an EOS GmbH (Germany) M290 industrial-grade L-PBF system using high purity (>99%) Ag and Cu powders supplied by Legor and Carpenter Additive, respectively. The L-PBF system features a 400 W laser system with 100 µm spot size where the laser melting process is carried out in an argon atmosphere at oxygen content below 0.1% at a substrate temperature of 35°C. Following fabrication, all samples were removed from the build platform using non-contact Electrical Discharge Machining (EDM).

Investigation of the pore morphology and its distribution is crucial for understanding the effects of L-PBF processing on the material performance and failure criteria. Accordingly, industrial metallurgy grinding, and polishing techniques (Struers United Kingdom) combined with Zeiss (Germany) SEM analysis were used to study Cu and Ag sample density and pore morphology. Ag and Cu porosity void type and distribution were characterised using SEM and stream essentials software. L-PBF process parameters listed in Table 1 developed by the authors in previous studies were used for sample fabrication and were kept constant to ensure any variation in pore morphology and distribution were a direct result of powder feedstock and material alone.

Table 1. L-PBF process parameters used for silver and copper sample fabrication.

Laser Power	Scan Speed	Hatch Distance	Layer Thickness
370 W	400 mm/s	0.14 mm	30 µm

2.2. Powder characterisation

Powder morphology and particle distribution can affect the packing density and flowability of L-PBF powders [50] dictating their behaviour during the process [50,51]. Therefore, the elemental analysis of Cu and Ag feedstock along with their morphology and particle volume distribution (PVD) were characterised using SEM and digital imaging particle analysis techniques. A Retsch Technology (Germany) Camsizer X2 was used to validate the particle morphology, size, and shape. The Camsizer X2 utilises dynamic image analysis (ISO 13322-2 [52]) principles where a high-resolution optical system consisting of digital cameras captures precise particle characteristics at a rate of 300 images per second. In depth CuAg powder analysis and characteristics have been reported in previous studies [49] while Fig. 1a and Fig. 1b display the SEM data showing the powder morphology for pure Ag and Cu powders, respectively.

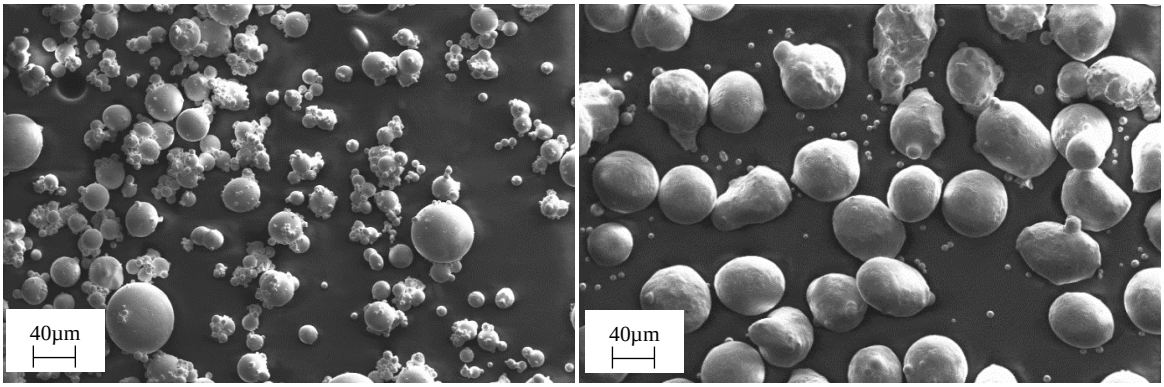

Fig. 1. Scanning Electron Microscopy (SEM) data showing particle morphology for (a) silver (b) copper feedstock.

It can be seen from the SEM data that while Ag and Cu particles feature a relatively spherical morphology the particle size varies. Ag features an even distribution of particle size and a larger distribution of powder particles below 20 µm with visible satellite particles. In comparison, most pure Cu particles are above 20 µm with some fine particles also visible. In general, Fig. 1 highlights the spherical morphology of Ag and Cu powder particles that is desired for the L-PBF process to enhance both the packing density and powder flowability [50].

Energy Dispersive X-Ray Spectroscopy (EDX) analysis was carried out using a Zeiss EVO50 SEM to confirm powder elemental composition. The resulting EDX spectra data are shown in Fig. 2a and 2b with elemental wt.% for Cu, Ag and CuAg alloys [49] summarised in Table 2. Ag and Cu powders were shown to be 99.73% Ag and 99.08% Cu respectively with balance oxygen.

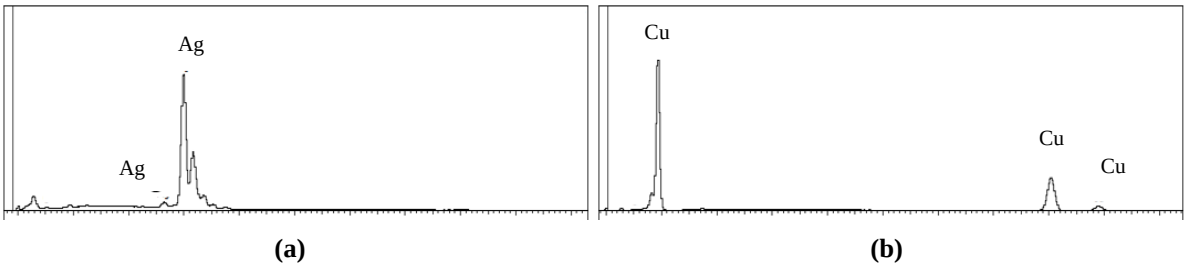

Fig. 2. Energy Dispersive X-ray (EDX) element spectra for the feedstock powder where (a) shows Ag and (b) Cu.

Table 2. Element composition of Ag, Cu and CuAg feedstock derived from their respective EDX spectrums.

Material	Element	Weight (%)
99.9% Silver	Ag	99.73
99.9% Copper	Cu	99.08
Copper-silver	Cu Ag10	Cu92.51 Ag7.49
Copper-silver	Cu Ag20	Cu72.50 Ag27.5
Copper-silver	Cu Ag30	Cu64.20 Ag35.8

Excessively high or low particle distribution can affect the powder flowability at the powder bed making it challenging for laser processing. Therefore, the quality of particle distribution was characterised using

dynamic image particle analysis to distinguish the mode, mean, median, and volume fractions (D_{10}, D_{50}, and D_{90}) and to identify the particle volume distribution (PVD). Fig. 3 displays the cumulative distribution of powder particles for Ag (Fig 3a) and Cu (Fig 3b).

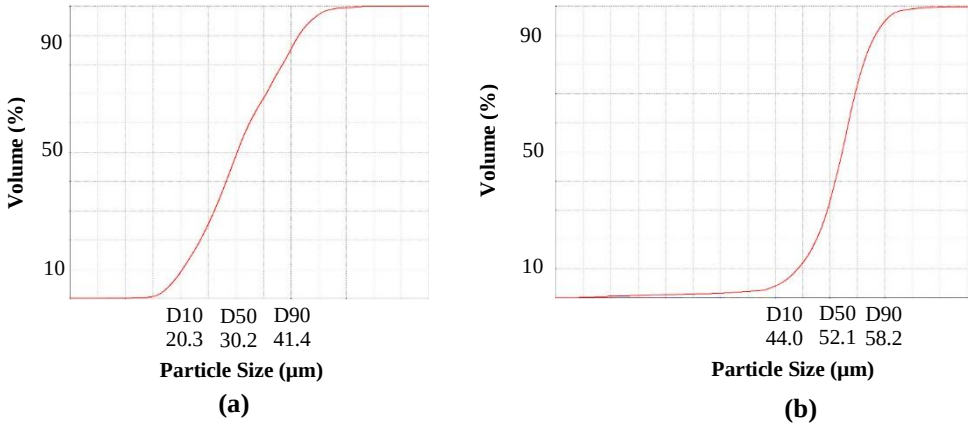

Fig. 3. Particle volume distribution for (a) Ag powder and (b) Cu powder.

The PVD analysis concluded Ag as having a D_{10} of 20.3 µm, D_{50} of 30.2 µm, and D_{90} of 41.4 µm while Cu featured a PVD of D_{10} of 44.0 µm, D_{50} of 52.1 µm, and D_{90} of 58.2 µm. A D_{90} of 10 µm can result in unusable powder for L-PBF processing [53], the PVD displayed in Fig. 3a and 3b, therefore, suggests that the Ag and Cu powders measured in this study have relatively even distributions and are suitable for L-PBF.

In addition to chemical composition, the size and shape of the powder particles are also of vital importance when it comes to L-PBF processability. Compared to optical microscopy, the dynamic image analysis technique allows measurement data of a large number of particles and is therefore statistically more relevant and offers better reproducibility. Dynamic image analysis of Ag and Cu powders were carried out with the resulting data sample as shown in Fig. 4a and 4b respectively. The typical particle size and shape are shown where the X_{max}, X_{min}, and X_{area} are the particle length, width, and equivalent diameter. The equivalent diameter of the particle is calculated by the diameter of a circle having the same projection area (A) and is useful for laser diffraction analysis comparison. X_{area} can be represented by equation 1.

$$X_{area} = \sqrt{\frac{4A}{\pi}}$$

Eq.1. X_{area} equivalent diameter equation.

As can be seen from Fig. 4a, Ag particles were relatively irregular in shape indicating the presence of satellite particles while Cu powder (Fig. 4b) were found to vary less between X_{max} and X_{min} indicating a relatively spherical shape.

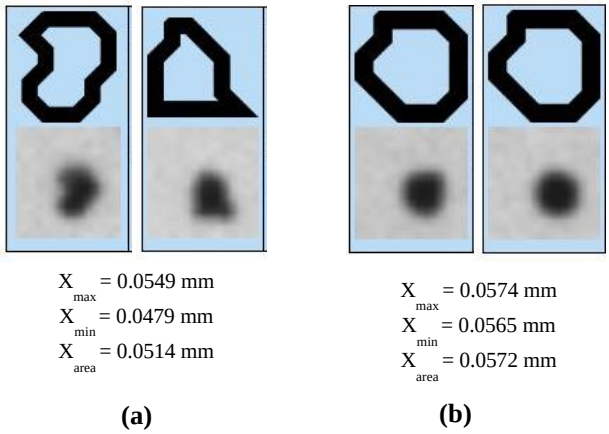

Fig. 4. Typical particle morphology and characteristics for (a) Ag powder and (b) Cu powder

2.3. Mechanical testing

Quasi-static tensile tests were carried out using a Zwick Roell (United States) 1474 universal testing machine having a maximum load capacity of 100 kN. The tests were conducted at room temperature and samples were strained to failure through a displacement-controlled load at a rate of 0.06 mm/s. A maximum load of 80 kN with a force shutdown threshold of 50% was applied. A deformation-controlled load was applied to prevent the test from stalling to capture both the elastic and plastic region of the material. Real-time force-displacement ($f - \delta$) and stress-strain ($\sigma - \varepsilon$) curves were recorded and analysed.

2.4. X-ray Computed Tomography

X-ray Computed Tomography (XCT) is a non-destructive analysis technique, which is seeing increasing use for AM pore defect investigation [54,55]. Incorrect powder feedstock properties such as PVD and poor flowability can lead to nonuniform powder layer delivery and porosity defects. However, pore defects can also result from laser and material interaction and process and scanning parameters used [56]. XCT analysis in this study was conducted utilising a Bruker (United States) Skyscan 2211 X-ray nano-tomograph. While XCT sample analysis is a valuable tool for non-destructive pore defect analysis the results achieved are dependent on the scanning and threshold parameters set by the operator. Therefore, XCT techniques are better utilised for comparative rather than absolute analysis. Comparative analysis ensures XCT scanning, and threshold parameters remain constant and therefore any variations in density and porosity defects can be attributed to L-PBF feedstock material, process parameters or post-processing used. In this regard, all samples were processed and scanned under

identical XCT scanning and threshold parameters so that the reconstructed data can be used to identify any notable changes in porosity as a result of powder characteristics or laser processing.

3. Results and discussion

3.1. Print quality and defect characterisation

3.1.1. Two-dimensional characterisation

To limit process variables all the samples were fabricated in the same orientation and build direction as shown in Fig 5.

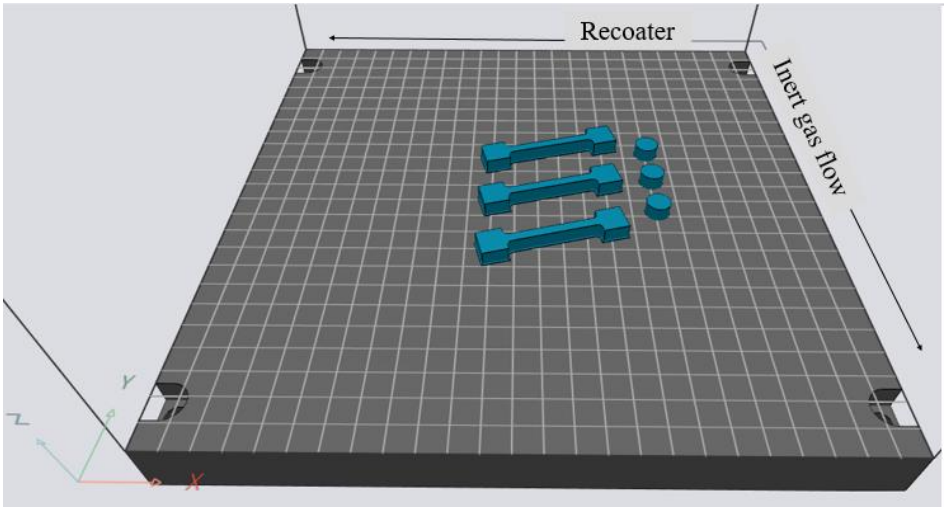

Fig. 5. Schematic showing tensile and thermal sample build orientation and recoater and inert gas flow direction.

Following the standard practice, the density and porosity content of the printed samples were evaluated using SEM data of polished Ag and Cu samples as shown in Fig. 6a and Fig. 6b respectively. Even though irregularly shaped pores were found for both the materials being studied, Cu was found to exhibit comparatively larger pore defects as shown in Fig. 6b. Overall, the porosity for pure Ag was evaluated at 2.78% with the highest pore size of 483 µm. In comparison, pure Cu exhibited both significantly higher porosity and pore size of 7.60% and 690 µm respectively.

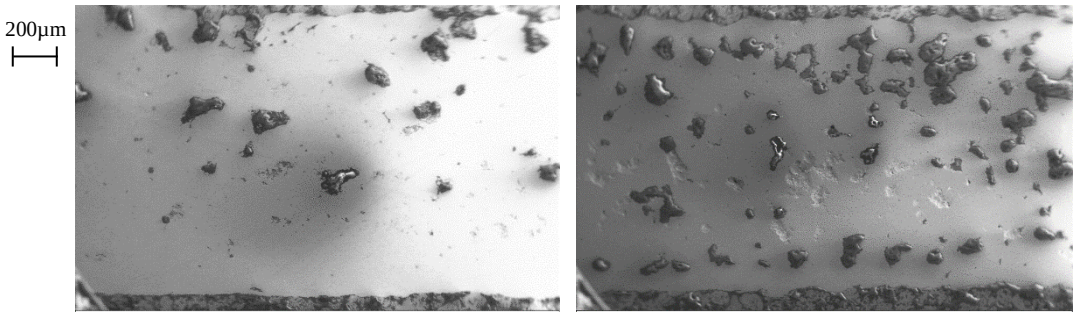

(a) **(b)**

Fig. 6. SEM data of polished cross-section (Z view) of the printed samples showing (a) Ag and (b) Cu.

Generally, a reduction in yield strength and reduced elongation to failure is a direct result of increasing pore size [56,57]. This can be true for porosity associated with L-PBF Ag and Cu parts as well, nevertheless, it is important to recognise that SEM data only shows pores at the two-dimensional (2D) layer that is being investigated. This means that other layers can feature different pore distribution and morphology which can cause variation in mechanical performance. Therefore, a complete understanding of the three-dimensional volumetric pore data within the parts is critical to understand its influence on the resulting mechanical performance. Accordingly, to understand the overall distribution of the porosity XCT investigation was conducted.

3.1.2. Reconstruction of volumetric porosity based on X-ray CT data

While traditional SEM analysis as shown in Fig. 6 is useful in establishing layer-based porosity of the printed samples they offer limited information on its distribution throughout the sample. XCT analysis enables the creation of three-dimensional data regarding both the porosity, pore morphology and distribution. XCT not only allows identifying areas of density variation in the sample but also allows comparison of defects. This aspect is feasible in this study due to the material compatibility with the process parameter used. While it is agreed that such a comparison using vastly dissimilar material may not offer further insights; for the study under consideration the process parameters are suitable to L-PBF process both Cu and Ag. The reconstructed X-ray 3D scan data for laser processed Ag and Cu samples are shown in Fig. 7a and Fig. 7b respectively with their density and pore count summarised in Table 3. A region of interest was selected in the centre of each sample allowing the highest resolution for XCT comparative analysis. Additionally, the regions of interest enable precise pore isolation and density investigation to be completed where XCT scanning of the whole sample would result in lower resolution. Previous in depth CuAg porosity and pore defect analysis and characterisation have been reported in previous studies [49] following the same XCT scanning process procedure.

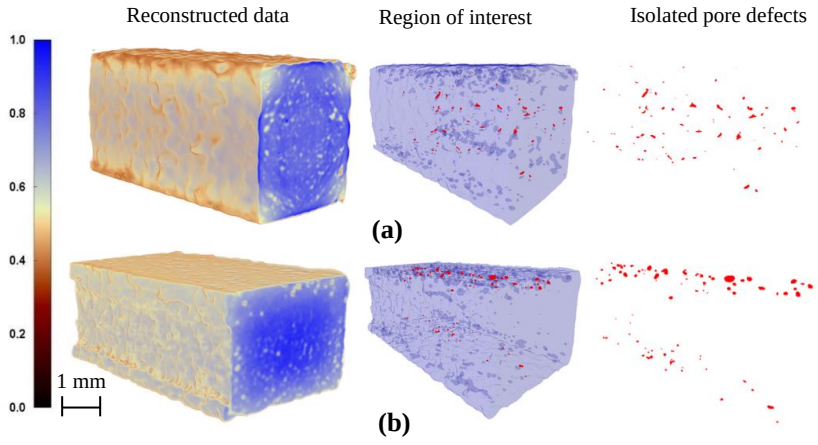

Fig. 7. XCT 3D visualisation showing the reconstructed data, region of interest along with porosity content and distribution of the L-PBF samples showing (a) Ag and (b) Cu. The contour represents X-ray absorption weighted for material density.

Table 3. Bulk density and the number of porosity defects for L-PBF Ag and Cu samples characterised through XCT data.

Material	Bulk density (%)	Closed pore count
Ag	99.9	90
Cu	99.8	130

The 3D reconstruction of the X-ray data was given an arbitrary colour grading showing the relatively dense material (high X-ray absorption) represented by 1 (blue) and 0 (black) representing no X-Ray absorption and therefore potential porosity voids. Closed pore porosity voids were then isolated and can be seen highlighted in red in Fig. 7. Although the data shows that there are porosity defects in both the samples a difference in both pore morphology and distribution can be observed. To further investigate the porosity distribution and to identify any trends the Z plane and X plane were isolated from the XCT data as shown in Fig. 8.

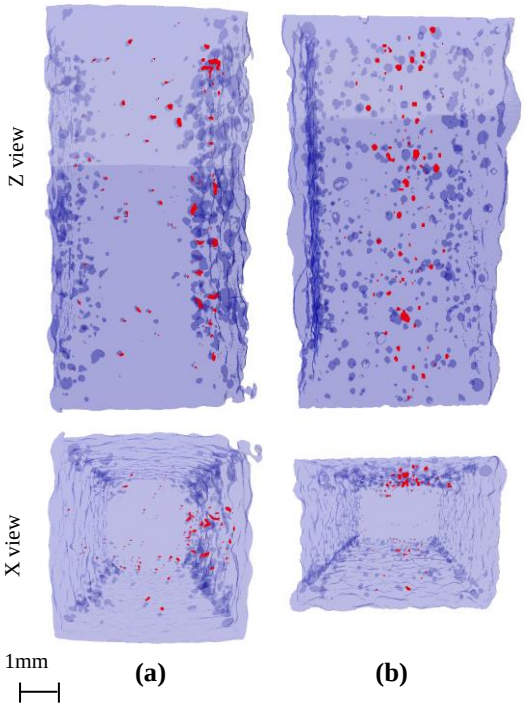

Fig. 8. XCT data of porosity content and distribution for printed samples in Z and X planes for (a) Ag and (b) Cu.

The sliced data shows that while Cu (Fig. 8b) has larger pores, the defects are largely confined to the top of the sample where 2D SEM analysis was conducted. Furthermore, the pore defects for Cu can also be seen to be confined to certain regions within the sample which is a result of poor powder delivery or packing density rather than incorrect parameters or laser-material interactions. In comparison, the Ag sample (Fig. 8b) was found to exhibit evenly distributed irregular morphology porosity throughout the sample which indicates that the pore defects are a result of lack of fusion referring to non-optimum process parameters. Although irregular particle morphology and satellite particles were seen in Fig. 1a and 4a this also raises questions regarding the powder packing density for the Ag material. As such the overall pore defects of pure Ag can be attributed to an interaction of powder quality and process

parameters. Cu on the other hand features a dense core with uniform porosity distributed along the edges. As such the X-ray tomography data highlight the importance of non-destructive XCT analysis to ascertain a true understanding of defects throughout L-PBF fabricated components.

3.1.3. Pore morphology and distribution

Although the pore defects in L-PBF Ag are irregular in shape they are evenly distributed along the scanned volume. On the contrary, the porosity observed in Cu were found to be spherical and confined to specific areas and layers. A comparative evaluation of pore sizes using the XCT in X, Y and Z build views are shown in Fig. 9. It can be seen that Ag features evenly distributed irregular pore morphology which is consistent with a lack of fusion porosity. This suggests that these pore defects were created during the L-PBF process attributable to the influence of both laser processing and the subsequent thermo-mechanical behaviour of the Ag melt pool. Contrastingly, for Cu, the spherical nature of the pores means that they are consistent with blowhole or keyhole porosity [56]. Generally, such defects are a result of gas entrapment during the L-PBF process, which may indicate a lower packing density at the powder bed; an aspect attributable to the relatively larger powder particles (Fig. 1b).

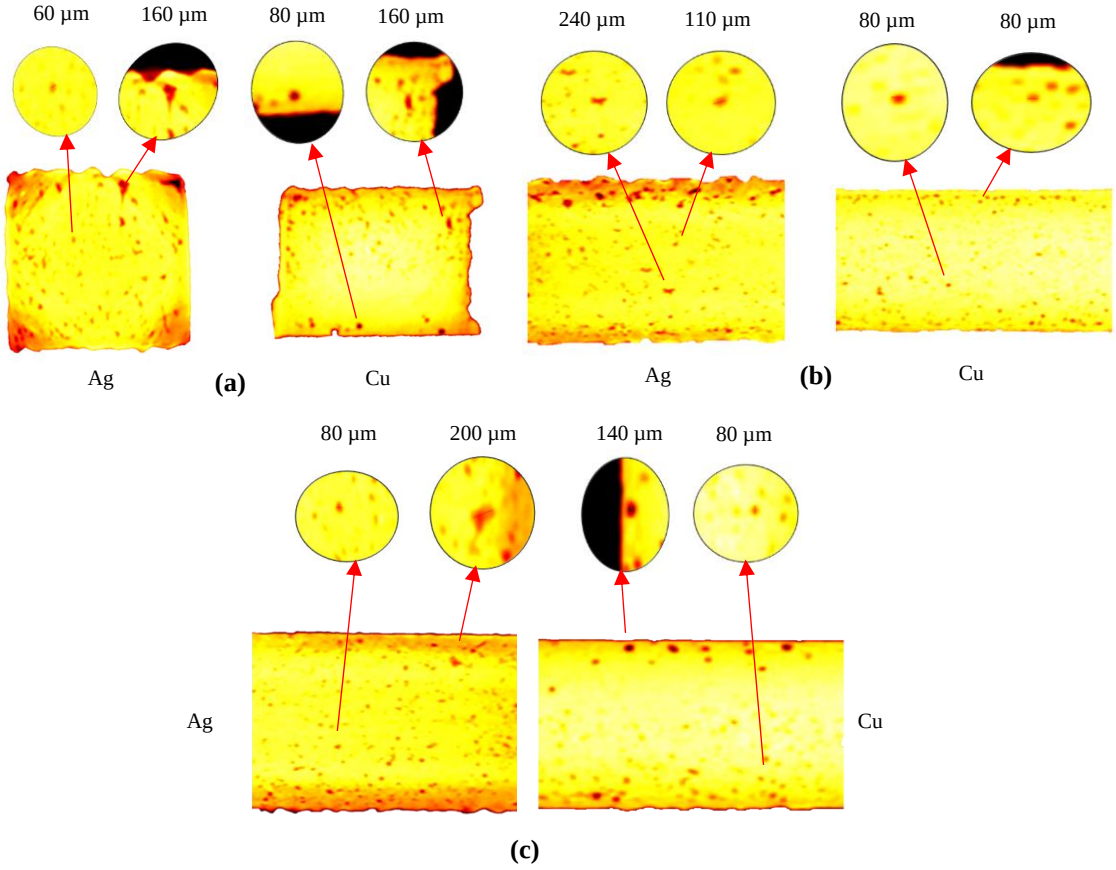

Fig. 9. Comparison of pore morphology between laser processed Ag and Cu samples showing using X-ray CT scan data were (a) X plane, (b) Y plane and (c) Z plane.

When the packing density of metal powders at the powder bed is low, the gas present between the powder particles dissolves in the melt pool during the laser melting process. The subsequent high cooling rate of the melt pool during the solidification process prevents the dissolved gas from resurfacing resulting in porosity in the fabricated part. However, as the pores seen here in the Cu sample are isolated to certain regions it is possible that poor powder distribution and delivery to the build plate during the process could also be responsible.

Due to the numerous feedstock and process variables [29] consistency and repeatability for quality control is an ongoing challenge for the AM industry particularly for L-PBF operators in the heavily regulated aerospace and medical sectors. Currently no agreed laser calibration techniques exist between system manufacturers and therefore materials and parameters must be developed for each system [58]**.** Generally, the strength, surface finish, density and microstructure of a component can all be affected by variations in the feedstock materials and L-PBF process and therefore to fabricate components with predictable thermal and mechanical properties a comprehensive understanding of material feedstock, L-PBF process and laser-material interactions is essential [7,59]. Furthermore, L-PBF variations due to feedstock have also been shown to promote porosity defects [56,60] affecting structural integrity leading to material failure [61,62].The type of porosity featured in the L-PBF Ag and Cu materials show that despite the similarity in the thermo-mechanical behaviour the differences in porosity type suggests that different approaches are needed to improve the density and reduce pore defects. For Ag, improved powder morphology with reduced satellite particles could improve powder packing density and further parameter optimization improve fusion [63]. For Cu an improvement in packing density and build chamber constraints such as different inert gas mixtures and oxygen and contamination reduction could be suitable to reduce gas entrapment porosity [64,65]. The high melt pool temperature as a result of the intense energy density required for highly reflective materials such as Ag and Cu may have also aided pore defects. Generally, high process temperature aid gas solubility in the melt pool, which is inevitably introduced into the powder bed through the feedstock. As opposed to traditional SEM-based evaluation, pore analysis using XCT in the way that is demonstrated in this study allows for further refinement of the processing parameters required for a denser part. As can be seen the quality and pore content of resultant L-PBF parts varies with material feedstock which can subsequently affect the mechanical performance of the materials. The subsequent section explores the mechanical properties of L-PBF Ag and Cu and in situ alloyed novel CuAg alloys using destructive testing.

3.2. Mechanical performance

Porosity defects in laser processed materials can result in stress concentration leading to premature failure where both the size and morphology of the porosity influence the magnitude of stress being generated. If the stress due to stress raisers exceeds the yield strength of the bulk material plastic deformation occurs leading to crack propagation and failure. Fig. 10. presents the stress-strain ($\sigma - \varepsilon$)

curve obtained for L-PBF processed Ag, Cu and CuAg alloys [49] under quasi-static loading with the resulting parameters of mechanical performances summarised in Table 4.

Evaluating the $\sigma - \varepsilon$ curve for L-PBF Ag and Cu samples revealed consistent elastic and plastic regions. It was found that Ag had significantly lower yield strength (σ_y) and ultimate tensile strength (UTS) in comparison to Cu. Cu L-PBF processed in this study exhibited a σ_y of 161.04 MPa which is comparable to commercially available EOS CuCrZr (160 MPa) and EOS CuCP (165 MPa) however, exhibited an 11% reduction in σ_y when compared to EOS Cu (180 MPa). Contrastingly Cu had comparable UTS (197.1 MPa) with EOS Cu (200 MPa) but exhibited a reduction in UTS of 16% and 6% relative to EOS CuCP and EOS CuCrZr. The corresponding σ – ε data for Ag, Cu, CuAg alloys and commercially available Cu shows a promising trend where the CuAg alloys consistently exhibit higher stiffness and strength with the addition of Ag.

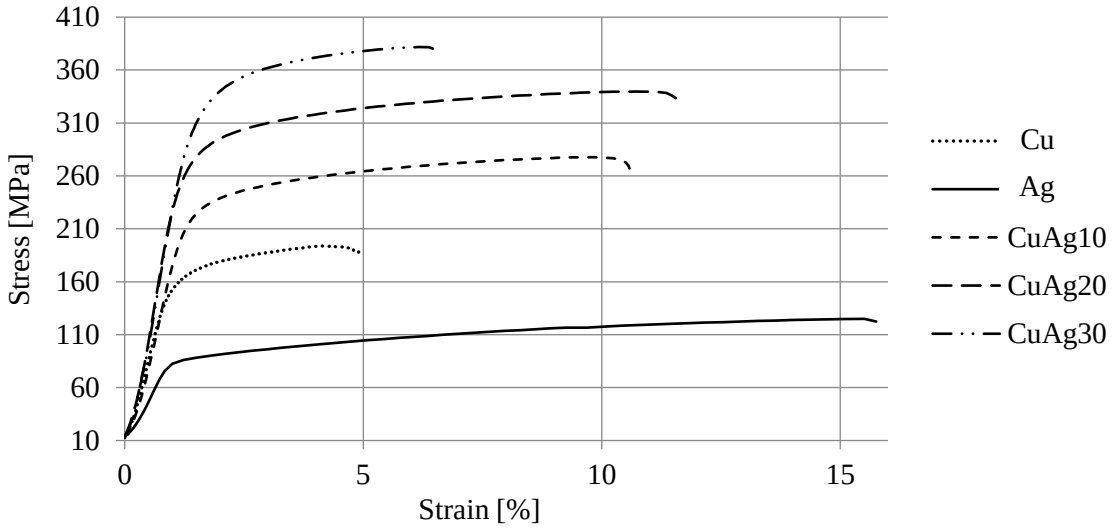

Fig. 10. Stress-strain curves obtained for as-built L-PBF pure Ag, pure Cu and CuAg alloys [49].

Table 4 summarises the parameters for mechanical performance obtained for Ag (a), Cu (b), CuAg alloys (c, d and e) and compares them to commercially available L-PBF Cu variants (f, g and h). Previous studies have demonstrated [49] the mechanical performance enhancements of Ag addition in Cu due to stronger binding effects at the CuAg interfaces reducing dislocation movements. However, no data is available or has been reported previously that comparatively analyses L-PBF Ag and Cu and/or commercially available L-PBF Cu materials.

Table 4. Summary of mechanical performance exhibited by L-PBF Ag, Cu, CuAg alloys [49] and EOS Cu alloys [47] where E, σ_y, ε_f and UTS are Young's modulus, yield strength, failure strain and ultimate tensile strength respectively.

Identifier	Material	E (Gpa)	σ_y (MPa)	ε_f (%)	UTS (MPa)
(a)	99.9% Ag	15.6	77.1	15.4	124.9
(b)	99.9% Cu	18.3	161.0	5.1	197.1
(c)	CuAg10%	18.4	223.5	8.1	277.7
(d)	CuAg20%	22.7	275.5	9.1	339.8
(e)	CuAg30%	24.3	330.3	4.4	381.8
(f)	EOS Cu	-	180	5	200
(g)	EOS CuCP	-	165	45	235
(h)	EOS CuCrZr	-	160	40	210

Comparing the mechanical performance parameters Fig. 11 displays significant, consistent, and almost linear increases in σ_y (Fig. 11a) and UTS (Fig. 11c) with increased Ag addition to Cu. The highest σ_y and UTS values were exhibited by the highest Ag content alloy CuAg30%. 10% Ag addition saw σ_y and UTS properties of 223.5 MPa and 277.7 MPa respectively. These values are 39% and 41% increases in comparison to Cu. 20% Ag addition saw increases of 75% and 72% from Cu to a σ_y of 275.5 MPa and UTS of 339.8 MPa while 30% Ag addition exhibited 105% and 94% increases. Evaluating the mechanical performance of commercially available Cu also saw CuAg alloys outperforming by 24%, 53% and 83% for σ_y and 18%, 45% and 63% for UTS with each 10% addition of Ag. The mechanical performance data discussed demonstrates the enhancement potential for L-PBF processing Cu and CuAg alloys.

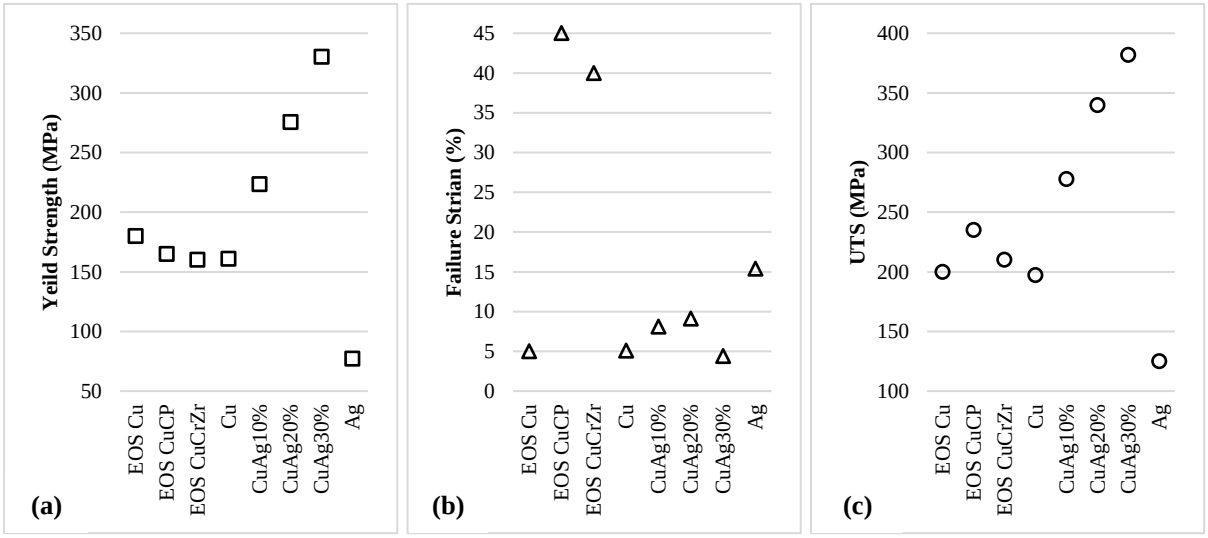

Fig. 11. Mechanical performance of industry Cu alloys [47], L-PBF Cu, Ag and influence of increasing Ag content on the mechanical performance of CuAg alloys [49] showing (a) yield strength, (b) failure strain and (c) ultimate tensile strength.

3.3. Thermal Performance

3.3.1. Density and pore defect characterisation

Thermal management and heat transfer materials are seeing increasing demand in various industries where recent research has reported heat transfer enhancements through L-PBF heat exchangers featuring complex lattices and honeycomb structures using AlSi10Mg and stainless steel materials [66,67]. Materials like aluminium-copper (AlCu) and copper-Yttrium (CuY) manufactured through laser depositing, casting and powder metallurgy [68–70] have also seen investigation reporting improvements in thermal diffusivity due to microstructure grain refinement through post-processing [69,70].

L-PBF material microstructure can vary depending on build orientation due to the layer-by-layer process, which influences material properties including thermal performance. Nevertheless, pore defects have been reported to have a negative effect on thermal conductivity for L-PBF materials an area that requires further studies [71]. Until now the thermal diffusivity of L-PBF materials has seen little research with no studies reporting the thermal diffusivity of highly conductive L-PBF materials. As such this study investigates the thermal diffusivity of L-PBF Ag, Cu and CuAg alloys considering the pore defects. Fig. 12 shows the L-PBF thermal test samples fabricated using Ag, Cu and CuAg. Although all samples were fabricated with the same parameters and had visibly similar surface finish there was colour variation representative of the associated Ag content.

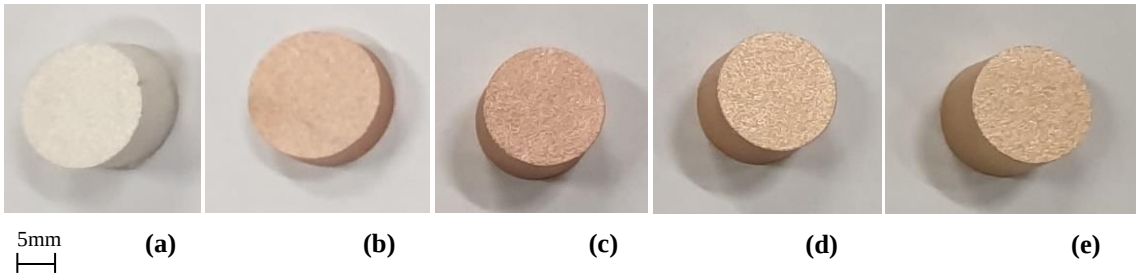

Fig. 12. *L-PBF thermal diffusivity samples showing (a) Ag, (b) Cu, (c) CuAg10%, (d) CuAg20% and (e) CuAg30%.*

The thermal properties of a material are affected by material density [72] and porosity [71]. Accordingly, XCT analysis and 3D visualisation were utilised to ascertain comparative sample density and porosity. Fig. 13. Shows the XCT 3D visualisations for L-PBF Ag, Cu and CuAg alloys with a summary of bulk density and porosity presented in Table 5.

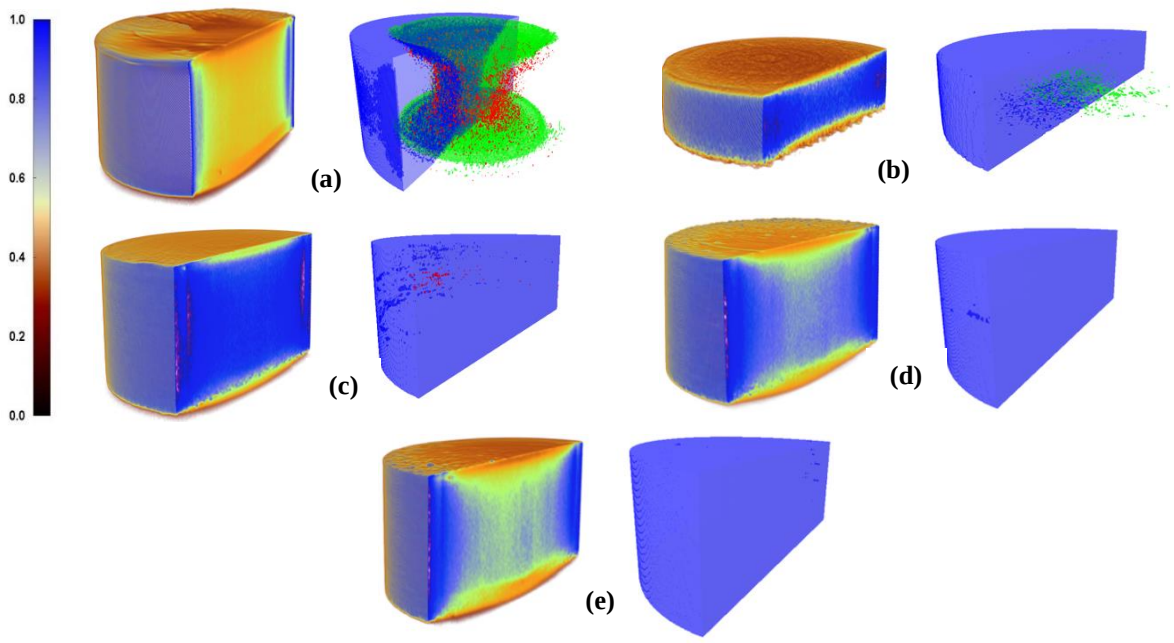

Fig. 13. XCT pore defect 3D visualisation for L-PBF thermal samples showing (a) Ag (b) Cu, (c) CuAg10%, (d) CuAg20% and (e) CuAg30%.

Table 5. XCT porosity and pore defect properties for L-PBF pure Ag and Cu thermal samples.

Material	Bulk density (%)	Number of closed pores
Pure Ag	89.9	9737
Pure Cu	99.9	56
CuAg10	100	173
CuAg20	100	1
CuAg30	100	0

Due to XCT scanning parameters and material similarity, comparative density results in Table 5 were found to be identical for all CuAg alloy compositions with a representative density of 100%. Additionally, very little variation to Cu was displayed with a representative density of 99.9%. However, Ag exhibited significant porosity resulting in a density of 89.9% featuring 9737 closed pores. Although density values for Cu and CuAg alloys are comparable evaluating the number of pores gives a clearer picture regarding material density. Overall, the trend establishes that the addition of Ag above 20% has a significant effect on the number of pores defined within the samples. 30% Ag exhibited the best sample with no pores in comparison to 20% Ag exhibiting one detectable pore. Cu pore content was 56 while 10% Ag displayed 173 detectable pores. Porosity content was isolated and highlighted in red and green to aid visualisation (Fig. 13) which further confirms the potential for CuAg alloys in achieving higher density.

3.3.2. Thermal Diffusivity

To evaluate the thermal performance of the material thermal diffusivity measurement analysis for L-PBF Ag, Cu and CuAg samples were conducted using Netzsch LFA [71]. Comparative measurements were conducted at room temperature with three repeating measurements the average of which are reported in Fig. 14c, while Fig. 14a and Fig. 14b compared the number of closed pore and density to take its influence into account.

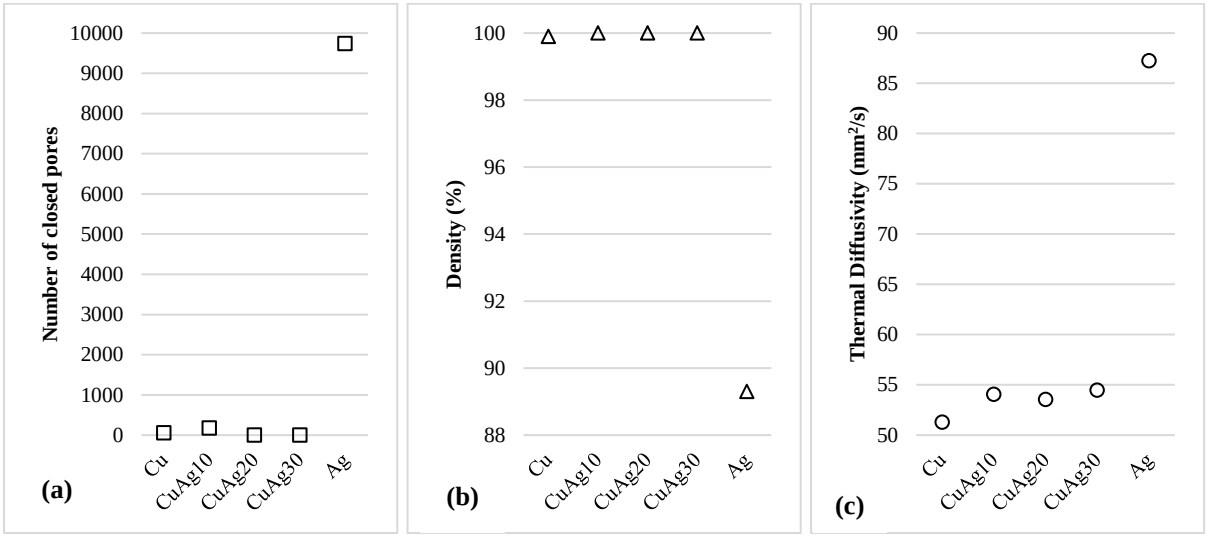

Fig. 14. XCT pore defect and thermal diffusivity data for L-PBF as-built Cu, CuAg10%, CuAg20%, CuAg30% and Ag samples showing (a) number of closed pore defects, (b) density and (c) thermal diffusivity.

Cu thermal diffusivity saw an increase of 5.3% with the addition of 10% Ag from 51.28 mm^2/s to 54.04mm^2/s. However, increasing Ag content further to 20% and 30% resulted in a 0.8% decrease followed by a 0.8% increase. Overall Ag content from 10% to 30% demonstrated a 0.8% variation on thermal diffusivity. The maximum variation between Cu and any CuAg alloy was 6.2% while Ag with the highest average pore size and relatively high number of pores to CuAg alloys displayed a minimum and maximum increase in thermal diffusivity of 60% and 63% respectively. Comparing thermal diffusivity results with XCT pore data it can be seen that material has a greater impact on thermal diffusivity than sample pore content and density. Ag exhibited 70% higher thermal diffusivity performance in comparison to Cu.

4. Prospects for L-PBF Cu alloys

Recent developments in computer-aided simulation, design tools [39,73], custom materials [28,74] and advanced manufacturing techniques [75,76] allows identifying novel techniques to solve complex problems that transcend the limitations associated with traditional manufacturing. Combining functional materials with regenerative design and L-PBF is already driving innovations in custom materials and

manufacturing. For example, Additive Analytics, Alloyed, Elementum 3D and M4P are all relatively new companies that are developing novel metallic materials and Metal Matrix Composites (MMC) for metal L-PBF processes.

The new generation of emerging design tools, materials and manufacturing technologies is being exploited by numerous industries for application-specific solutions. For example, a high-performance Cu alloy was developed by AMCM for the largest 3D printed rocket combustion chamber. In doing so Launcher reduced cost, lead time and part complexity fabricating a single piece chamber that enabled the highest performance liquid rocket engine to aid the development of the world's most efficient rocket launcher for small satellite systems.

Additive Drives utilises high powered L-PBF systems and high purity copper to fabricate high-efficiency windings for electric motors. Achieving electrical conductivity of 100% International Annealed Copper Standard (IACS) combined with the design and manufacturing freedoms of L-PBF is driving a new era in 3D printing electric motors. Conflux Technologies utilises L-PBF to fabricate high-performance heat exchangers that are challenging to be manufactured through traditional fabrication techniques resulting in performance enhancement in heat transfer and pressure drop by three times at a 50% reduced weight. The examples discussed thus far emphasise the increasing trend regarding application-specific materials that can be processed using L-PBF for high-performance components and systems. It is also worth noting that Ag and Cu materials also exhibit desirable antimicrobial and electrical conductive properties [31,77,78] and as such are of interest for applications such as renewable energy, biomedical and electronics [79–81].

5. Conclusions

The study investigated the L-PBF processing of high purity (>99%) Ag, Cu and CuAg alloys characterising the material porosity morphology along with their mechanical and thermal performance. The study identified a potential parametric combination that enables the laser processing of high purity Ag, Cu and CuAg alloys using a standard 400 W laser system. The X-ray CT data showed that Ag exhibited evenly distributed irregular pore morphology signifying lack of fusion porosity while spherical pore morphology displayed in Cu signified isolated gas entrapment during the melt pool. This means that improved packing density and process parameter optimisation is required for both Ag and Cu. Looking at the material behaviour Ag exhibited higher failure strain yet significantly lower yield strength and UTS in comparison to Cu. Overall, L-PBF Cu had comparable yield strength (161.04 MPa) to commercially available EOS CuCrZr (160 MPa) and EOS CuCP (165 MPa) however exhibited an 11% reduction when compared to EOS Cu (180 MPa). Contrastingly L-PBF Cu had comparable UTS (197.1 MPa) with EOS Cu (200 MPa) but exhibited a reduction in UTS of 16% and 6% relative to EOS

CuCP and EOS CuCrZr. Nevertheless, Ag addition in Cu was found to drastically increase the yield strength and UTS significantly resulting in novel CuAg alloys outperforming both Ag, Cu and all commercially available Cu materials evaluated. As such the CuAg30% exhibits 84%, 100% and 106% higher yield strengths in comparison to commercially available Cu, CuCP and CuCrZr while UTS values were 91%, 62% and 82% higher. The Youngs Modulus for the novel CuAg composition were 33% higher in comparison to Cu. Unfortunately, Youngs Modulus data for industry-standard Cu alloys was not available for analysis. On the thermal performance, Ag outperformed Cu and CuAg alloys by 70% despite the significant porosity and lower density in comparison. Ag addition displayed minimal increases in thermal diffusivity values from Cu. Overall Ag content from 10% to 30% displayed a maximum 0.8% variation in thermal diffusivity. The maximum variation between Cu and any CuAg alloy was a 6.2% increase in thermal diffusivity. The work reported in this study demonstrates the potential for the development of high-performance CuAg alloys that outperform commercially available Cu. However, further research and investigation are required to optimise the processability and repeatability focusing on specific applications such as fatigue and elevated temperatures.

Acknowledgements

This research was conducted with support from the European Commission Research Grant 32R19P03053, University of Wolverhampton, Additive Analytics Ltd and EOS GmbH.

Data availability

The data that supports the findings of this study are available from the corresponding author upon reasonable request.

References

1. D. Jafari and W. W. Wits: The utilization of selective laser melting technology on heat transfer devices for thermal energy conversion applications: A review. *Renew. Sustain. Energy Rev.* **91**(March), 420 (2018).

2. T. Alam and M. H. Kim: A comprehensive review on single phase heat transfer enhancement techniques in heat exchanger applications. *Renew. Sustain. Energy Rev.* **81**(August 2016), 813 (2018).

3. A. Baroutaji, A. Arjunan, M. Ramadan, and A. Olabi: Advancements and prospects of thermal management and waste heat recovery of PEMFC. *Int. J. Thermofluids* 100064 (2021).

4. J. Garfield: Research Report. *Teach. Stat.* **16**(2), 60 (1994).

5. E. Sevinchan, I. Dincer, and H. Lang: A review on thermal management methods for robots. *Appl. Therm. Eng.* **140**(March), 799 (2018).

6. A. Arjunan, A. Baroutaji, A. S. Praveen, J. Robinson, and C. Wang: in *Ref. Modul. Mater. Sci. Mater. Eng.* (Elsevier, 2020).

7. L. Ventola, F. Robotti, M. Dialameh, F. Calignano, D. Manfredi, E. Chiavazzo, and P. Asinari: Rough surfaces with enhanced heat transfer for electronics cooling by direct metal laser sintering. *Int. J. Heat Mass Transf.* **75**, 58 (2014).

8. B. S. Lazarov, O. Sigmund, K. E. Meyer, and J. Alexandersen: Experimental validation of additively manufactured optimized shapes for passive cooling. *Appl. Energy* **226**(February), 330 (2018).

9. X. Chen, H. Ye, X. Fan, T. Ren, and G. Zhang: A review of small heat pipes for electronics. *Appl. Therm. Eng.* **96**, 1 (2016).

10. H. Wang, T. Tao, J. Xu, X. Mei, X. Liu, and P. Gou: Cooling capacity of a novel modular liquid-cooled battery thermal management system for cylindrical lithium ion batteries. *Appl. Therm. Eng.* **178**(June), 115591 (2020).

11. B. Li, J. Hong, L. Ge, and C. Xuan: Designing biologically inspired heat conduction paths for 'volume-to-point' problems. *Mater. Des.* **130**(May), 317 (2017).

12. Y. Pan, S. Wang, P. Mao, and C. Jin: Role of Si concentration on the thermodynamic properties of molybdenum silicides. *Vacuum* **141**, 170 (2017).

13. S. M. Thompson, Z. S. Aspin, N. Shamsaei, A. Elwany, and L. Bian: Additive manufacturing of heat exchangers: A case study on a multi-layered Ti-6Al-4V oscillating heat pipe. *Addit. Manuf.* **8**, 163 (2015).

14. N. H. Naqiuddin, L. H. Saw, M. C. Yew, F. Yusof, T. C. Ng, and M. K. Yew: Overview of micro-channel design for high heat flux application. *Renew. Sustain. Energy Rev.* **82**(February 2017), 901 (2018).

15. E. M. Dede, S. N. Joshi, and F. Zhou: Topology Optimization, Additive Layer Manufacturing, and Experimental Testing of an Air-Cooled Heat Sink. *J. Mech. Des.* **137**(11), 111403 (2015).

16. J. K. Wohlers Associates. Terry Wohlers, Ian Campbell, Olaf Diegel, Ray Huff: Wohlers Report 2020 (2020).

17. T. D. Ngo, A. Kashani, G. Imbalzano, K. T. Q. Nguyen, and D. Hui: Additive manufacturing (3D printing): A review of materials, methods, applications and challenges. *Compos. Part B*

Eng. **143**(December 2017), 172 (2018).

18. C. L. Chia-Hung Hung, Wei.Ting, Chen, M. Hossein Sehhat and Ming: The effect of laser welding modes on mechanical properties and microstructure of 304L stainless steel parts fabricated by laser-foil-printing additive manufacturing. (n.d.).

19. N. Strategy: Additive Manufacturing UK. (2018).

20. Ernst & Young: EY's Global 3D printing Report 2016. *Ernst and Young* 1 (2016).

21. N. Li, S. Huang, G. Zhang, R. Qin, W. Liu, H. Xiong, G. Shi, and J. Blackburn: Progress in additive manufacturing on new materials: A review. *J. Mater. Sci. Technol.* **35**(2), 242 (2019).

22. F. Romei, A. N. Grubišić, and D. Gibbon: Manufacturing of a high-temperature resistojet heat exchanger by selective laser melting. *Acta Astronaut.* **138**, 356 (2017).

23. I. Yadroitsev, A. Gusarov, I. Yadroitsava, and I. Smurov: Single track formation in selective laser melting of metal powders. *J. Mater. Process. Technol.* **210**(12), 1624 (2010).

24. L. Zai, C. Zhang, Y. Wang, W. Guo, D. Wellmann, X. Tong, and Y. Tian: Laser powder bed fusion of precipitation-hardened martensitic stainless steels: A review. *Metals (Basel).* **10**(2) (2020).

25. H. Chen, C. Zhang, D. Jia, D. Wellmann, and W. Liu: Corrosion behaviors of selective laser melted aluminum alloys: A review. *Metals (Basel).* **10**(1) (2020).

26. Z. Tian, C. Zhang, D. Wang, W. Liu, and X. Fang: A Review on Laser Powder Bed Fusion of Inconel 625. *Appl. Scien* (2020).

27. V. S. Sufiiarov, A. A. Popovich, E. V. Borisov, I. A. Polozov, D. V. Masaylo, and A. V. Orlov: The Effect of Layer Thickness at Selective Laser Melting. *Procedia Eng.* **174**, 126 (2017).

28. J. Y. Lee, J. An, and C. K. Chua: Fundamentals and applications of 3D printing for novel materials. *Appl. Mater. Today* **7**, 120 (2017).

29. P. O'Regan, P. Prickett, R. Setchi, G. Hankins, and N. Jones: Metal Based Additive Layer Manufacturing: Variations, Correlations and Process Control. *Procedia Comput. Sci.* **96**, 216 (2016).

30. A. Gisario, M. Barletta, and R. Stancampiano: On the interaction mechanisms between a high-power diode laser source and silver alloys: The case of aesthetic welding. *Opt. Lasers Eng.* **47**(7–8), 821 (2009).

31. C. Silbernagel, L. Gargalis, I. Ashcroft, R. Hague, M. Galea, and P. Dickens: Electrical resistivity of pure copper processed by medium-powered laser powder bed fusion additive manufacturing for use in electromagnetic applications. *Addit. Manuf.* **29**(August), 100831 (2019).

32. M. Colopi, L. Caprio, A. G. Demir, and B. Previtali: Selective laser melting of pure Cu with a 1 kW single mode fiber laser. *Procedia CIRP* **74**, 59 (2018).

33. W. Xiong, L. Hao, Y. Li, D. Tang, Q. Cui, Z. Feng, and C. Yan: Effect of selective laser melting parameters on morphology, microstructure, densification and mechanical properties of supersaturated silver alloy. *Mater. Des.* **170**, 107697 (2019).

34. D. R. H. Jones and M. F. Ashby: Thermal Conductivity and Specific Heat. *Eng. Mater. 1* 515 (2019).

35. A. Sun, Z. Wu, X. Dong, B. Duan, and D. Wang: Effects of Ag addition on electrical and thermal properties of Mo–Cu composites. *J. Alloys Compd.* **657**, 8 (2016).

36. A. Popovich, V. Sufiiarov, I. Polozov, E. Borisov, D. Masaylo, and A. Orlov: Microstructure and mechanical properties of additive manufactured copper alloy. *Mater. Lett.* **179**, 38 (2016).

37. C. P. Wu, D. Q. Yi, W. Weng, S. H. Li, and J. M. Zhou: Influence of alloy components on arc erosion morphology of Ag/MeO electrical contact materials. *Trans. Nonferrous Met. Soc. China (English Ed.* **26**(1), 185 (2016).

38. S. Maharubin, Y. Hu, D. Sooriyaarachchi, W. Cong, and G. Z. Tan: Laser engineered net shaping of antimicrobial and biocompatible titanium-silver alloys. *Mater. Sci. Eng. C* **105**(December 2018), 110059 (2019).

39. M. Fateri, A. Gebhardt, J.-S. Hötter, M. Knothe, F. M. Schmidt, and H. Rieper: Numerical and Experimental Investigation of Selective Laser Melting of Silver. *Fraunhofer Direct Digit. Manuf. Conf. (DDMC), Berlin* No. February (2012).

40. J. Robinson, M. Stanford, and A. Arjunan: Stable formation of powder bed laser fused 99.9% silver. *Mater. Today Commun.* **24**(June 2019), 101195 (2020).

41. G. Abbas Gohar, T. Manzoor, and A. N. Shah: Investigation of thermal and mechanical properties of Cu-Al alloys with silver addition prepared by powder metallurgy. *J. Alloys Compd.* **735**, 802 (2018).

42. A. Sun, Z. Wu, X. Dong, B. Duan, and D. Wang: Effects of Ag addition on electrical and thermal properties of Mo-Cu composites. *J. Alloys Compd.* **657**, 8 (2016).

43. R. Guschlbauer, S. Momeni, F. Osmanlic, and C. Körner: Process development of 99.95% pure copper processed via selective electron beam melting and its mechanical and physical properties. *Mater. Charact.* **143**(March), 163 (2018).

44. A. Yan, Z. Wang, T. Yang, Y. Wang, and Z. Ma: Microstructure, thermal physical property and surface morphology of W-Cu composite fabricated via selective laser melting. *Mater. Des.* **109**, 79 (2016).

45. M. Wang, R. Li, T. Yuan, C. Chen, M. Zhang, Q. Weng, and J. Yuan: Selective laser melting of W-Ni-Cu composite powder: Densification, microstructure evolution and nano-crystalline formation. *Int. J. Refract. Met. Hard Mater.* **70**(May 2017), 9 (2018).

46. K. G. Cooper, J. L. Lydon, M. D. Lecorre, and Z. C. Jones: Three-Dimensional Printing GRCop-42. No. December 2018 (2019).

47. E. O. S. Copper, C. Eos, C. Cucp, and E. O. S. Copperalloy: It ‘ s Copper Time Material Data Sheets EOS Copper Cu. (n.d.).

48. Copper (AMCopper-100). **1269**, 80516 (2020).

49. J. Robinson, A. Arjunan, M. Stanford, I. Lyall, and C. Williams: Effect of silver addition in copper-silver alloys fabricated by laser powder bed fusion in situ alloying. *J. Alloys Compd.* No. xxxx, 157561 (2020).

50. J. H. Tan, W. L. E. Wong, and K. W. Dalgarno: An overview of powder granulometry on feedstock and part performance in the selective laser melting process. *Addit. Manuf.* **18**, 228 (2017).

51. A. Arjunan, M. Singh, A. Baroutaji, and C. Wang: Additively manufactured AlSi10Mg inherently stable thin and thick-walled lattice with negative Poisson’s ratio. *Compos. Struct.*

247(April), 112469 (2020).

52. ISO 13322-2: Particle size analysis — Image analysis methods — Part 2: Dynamic image analysis methods. *Int. Organ. Stand.* **2019**(40) (2006).

53. C. Pleass and S. Jothi: Influence of powder characteristics and additive manufacturing process parameters on the microstructure and mechanical behaviour of Inconel 625 fabricated by Selective Laser Melting. *Addit. Manuf.* **24**(May), 419 (2018).

54. J. Fieres, P. Schumann, and C. Reinhart: Predicting failure in additively manufactured parts using X-ray computed tomography and simulation. *Procedia Eng.* **213**, 69 (2018).

55. N. Ortega, S. Martínez, I. Cerrillo, A. Lamikiz, and E. Ukar: Computed tomography approach to quality control of the Inconel 718 components obtained by additive manufacturing (SLM). *Procedia Manuf.* **13**, 116 (2017).

56. M. Bayat, A. Thanki, S. Mohanty, A. Witvrouw, S. Yang, J. Thorborg, N. Skat Tiedje, and J. H. Hattel: Keyhole-induced porosities in Laser-based Powder Bed Fusion (L-PBF) of Ti6Al4V: High-fidelity modelling and experimental validation. *Addit. Manuf.* No. August, 100835 (2019).

57. F. Zanini, E. Sbettega, and S. Carmignato: X-ray computed tomography for metal additive manufacturing: Challenges and solutions for accuracy enhancement. *Procedia CIRP* **75**, 114 (2018).

58. J. Wright: Additive Manufacturing of Tungsten via Selective Laser Melting and Electron Beam Melting. 5 (2020).

59. D. Bourell, J. P. Kruth, M. Leu, G. Levy, D. Rosen, A. M. Beese, and A. Clare: Materials for additive manufacturing. *CIRP Ann. - Manuf. Technol.* **66**(2), 659 (2017).

60. J. Zhang, B. Song, Q. Wei, D. Bourell, and Y. Shi: A review of selective laser melting of aluminum alloys: Processing, microstructure, property and developing trends. *J. Mater. Sci. Technol.* **35**(2), 270 (2019).

61. S. Zhang, S. Rauniyar, S. Shrestha, A. Ward, and K. Chou: An experimental study of tensile property variability in selective laser melting. *J. Manuf. Process.* **43**(February), 26 (2019).

62. J. Clayton and R. Deffley: Optimising metal powders for additive manufacturing. *Met. Powder Rep.* **69**(5), 14 (2014).

63. Z. Snow, A. R. Nassar, and E. W. Reutzel: Invited Review Article: Review of the formation and impact of flaws in powder bed fusion additive manufacturing. *Addit. Manuf.* **36**(July), 101457 (2020).

64. C. Pauzon, P. Forêt, E. Hryha, T. Arunprasad, and L. Nyborg: Argon-helium mixtures as Laser-Powder Bed Fusion atmospheres: Towards increased build rate of Ti-6Al-4V. *J. Mater. Process. Technol.* **279**(March 2019), 116555 (2020).

65. C. Pauzon, K. Dietrich, P. Forêt, S. Dubiez-Le Goff, E. Hryha, and G. Witt: Control of residual oxygen of the process atmosphere during laser-powder bed fusion processing of Ti-6Al-4V. *Addit. Manuf.* **38**, 101765 (2021).

66. J. Y. Ho, K. C. Leong, and T. N. Wong: Additively-manufactured metallic porous lattice heat exchangers for air-side heat transfer enhancement. *Int. J. Heat Mass Transf.* **150** (2020).

67. D. Kong, Y. Zhang, and S. Liu: Convective heat transfer enhancement by novel honeycomb-core in sandwich panel exchanger fabricated by additive manufacturing. *Appl. Therm. Eng.*

163(September), 114408 (2019).

68. J. I. Arrizubieta, M. Cortina, A. Mendioroz, A. Salazar, and A. Lamikiz: Thermal diffusivity measurement of laser-deposited AISI H13 tool steel and impact on cooling performance of hot stamping tools. *Metals (Basel).* **10**(1) (2020).

69. A. G. Esmeralda, A. F. Rodríguez, J. Talamantes-Silva, R. Torres, N. F. Garza-Montes-de-Oca, J. R. Benavides-Treviño, and R. Colás: Thermal diffusivity of cast Al-Cu alloys. *Thermochim. Acta* **683**(October 2019), 178444 (2020).

70. G. Carro, A. Muñoz, M. A. Monge, B. Savoini, A. Galatanu, M. Galatanu, and R. Pareja: Thermal conductivity and diffusivity of Cu-Y alloys produced by different powder metallurgy routes. *Fusion Eng. Des.* **124**, 1156 (2017).

71. J. C. Simmons, X. Chen, A. Azizi, M. A. Daeumer, P. Y. Zavalij, G. Zhou, and S. N. Schiffres: Influence of processing and microstructure on the local and bulk thermal conductivity of selective laser melted 316L stainless steel. *Addit. Manuf.* **32**(October 2019), 100996 (2020).

72. I. A. Roberts, C. J. Wang, R. Esterlein, M. Stanford, and D. J. Mynors: A three-dimensional finite element analysis of the temperature field during laser melting of metal powders in additive layer manufacturing. *Int. J. Mach. Tools Manuf.* **49**(12–13), 916 (2009).

73. M. Vlahinos and R. O. Hara: Unlocking Advanced Heat Exchanger Design and Simulation with nTop Platform and ANSYS CFX. (2020).

74. Y. S. Jhong, H. T. Tseng, and S. J. Lin: Diamond/Ag-Ti composites with high thermal conductivity and excellent thermal cycling performance fabricated by pressureless sintering. *J. Alloys Compd.* **801**, 589 (2019).

75. J. Huang, X. Yan, C. Chang, Y. Xie, W. Ma, R. Huang, R. Zhao, S. Li, M. Liu, and H. Liao: Pure copper components fabricated by cold spray (CS) and selective laser melting (SLM) technology. *Surf. Coatings Technol.* (2020).

76. A. L. Moore and L. Shi: Emerging challenges and materials for thermal management of electronics. *Mater. Today* **17**(4), 163 (2014).

77. N. Simpson, D. J. North, S. M. Collins, and P. H. Mellor: Additive Manufacturing of Shaped Profile Windings for Minimal AC Loss in Electrical Machines. *IEEE Trans. Ind. Appl.* **56**(3), 2510 (2020).

78. A. Arjunan, J. Robinson, E. Al Ani, W. Heaselgrave, A. Baroutaji, and C. Wang: Mechanical performance of additively manufactured pure silver antibacterial bone scaffolds. *J. Mech. Behav. Biomed. Mater.* **112**, 1 (2020).

79. D. Bradley: Every silver-lined solar cell. *Mater. Today* **12**(11), 10 (2009).

80. N. Ciacotich, R. U. Din, J. J. Sloth, P. Møller, and L. Gram: An electroplated copper–silver alloy as antibacterial coating on stainless steel. *Surf. Coatings Technol.* **345**(April), 96 (2018).

81. A. Arjunan, A. Baroutaji, J. Robinson, A. S. Praveen, A. Pollard, and C. Wang: in *Ref. Modul. Mater. Sci. Mater. Eng.* (Elsevier, 2021).